

## OPTICAL CHARACTERIZATION OF THE LASER-INDUCED SPARK IN AIR

Phuoc X. Tran, and C.M. White  
U.S. Department of Energy  
National Energy Technology Laboratory  
Pittsburgh, PA. 15236  
phone: (412) 386-6024  
E-mail: [tran@netl.doe.gov](mailto:tran@netl.doe.gov)

### Abstract

This present work studies the formation of the laser-induced spark. Properties such the breakdown probability, spark absorption, spark temperature and spark evolution were investigated. Spark temperature was measured using the two-line intensity ratio technique. The absolute intensities emitted from O I at 748.07 nm and 777.54 nm were used. The beam deflection technique was used for spark evolution study. It was shown that the laser spark temperature in the order of  $10^5$  to  $10^6$  K could be reached at the end of the laser and that the focal length of the focusing lens had a strong effect on the breakdown probability, the spark energy and temperature. The evolution of the laser spark always involved with the formation and the propagation of the shock wave front, the expansion of the spark volume, the after-shock perturbation, and the complete shock detachment.

### 1. Introduction

When a laser beam with an irradiance  $\geq 10^{10}$  W/cm<sup>2</sup> interacts with a gas near atmospheric pressure, the gas breaks down owing to multiphoton ionization or electron avalanche [1-5]. As a result a high temperature and pressure spark is generated. The spark then rapidly explodes into a supersonic shock wave that propagates into the ambient gas. Sparks created this way have many practical applications. Especially, the use of the laser-induced breakdown for ignition offers many potential benefits over conventional ignition systems [6-13]. Past studies have shown that the laser ignition process depends ultimately on the generation of reactive species, the absorption (ignition) energy, the volume of the spark, and the spark evolution and interaction with the surrounding gases. These processes depend strongly on the initial gas breakdown event. However, as widely reported [1-4], laser-induced breakdown is a probabilistic process. For example, the threshold laser energy for initiating gas breakdown, which is strongly dependent on the gas pressure and the laser wavelength, can vary by more than a factor of two. Such large variations in the gas breakdown may cause fluctuations in the subsequent processes. These, in turn, can lead to instability in the chemical ignition process and significantly affect the overall combustion process and the yields of combustion products. Chen et al. [14] studied the ignition of a laminar flow of stoichiometric mixtures of ammonia and oxygen. They showed that the success or failure of an ignition event is due to the fluctuations of the spark energy and the intensity of the NH fluorescence signal, which are related very well with the fluctuation of the breakdown event. Laser ignition studies reported by Phuoc and White [13] and others [6-11] have shown that a successful ignition event requires not only sufficient spark energy but also an

optimum spark kernel radius to which the flame must grow after the spark energy is deposited. Thus, the fluctuation in both spark size and spark energy might result in an ignition failure if the spark size is not large enough to support the flame to grow or the deposited energy is less than the minimum ignition energy.

Thus, it is very important to examine the laser spark formation in terms of the breakdown probability, the spark absorption and evolution processes. Here report some preliminary measurements of the spatial distributions of the single-shot breakdown probability and the resulting spark energy, temperature, and evolution of the shock front in the quiescent air as functions of the laser and optical parameters.

## **2. Experimental Apparatus**

The experimental apparatus used in this study was described elsewhere [4,5]. In brief, it consisted of a single-mode, Q-switched Nd-Yag lasers (Quantel, Brilliant W) which was operated at 1064 nm wavelength and 5.5 ns pulse duration. The beam delivery optics had mainly a 1% to 99% variable beam splitter and a focusing lens. In order to have a well-controlled beam energy throughout the experiments, the laser potential controller was set at a fixed location and vary the beam energy by rotating the beam splitter about its center.

Two pyroelectric energy meters (Oriol 70713), together with two energy readout units (Oriol 70833) were used for spark energy measurements. One meter was placed behind the focal volume facing the incoming laser beam, and the other was placed after the variable beam splitter, which was located before the focusing lens.

For space-resolved measurements of the OI emission lines we used a Multichannel Instaspec IV CCD detection system (Oriol). It consisted of a front illuminated 1024 x 128 pixel format CCD detector head (Model 78430, Oriol), a MS260i imaging spectrograph (Model 74050, Oriol), a single-track fiber optic cable (Model 77403, Oriol), and a F-NO matcher (Model 77529, Oriol). The MS260i had a micrometer driven entrance slit with its width is variable from 4  $\mu\text{m}$  to 3 mm and its height is from 2 to 12 mm. It was equipped with three gratings covering a spectrum of 250 to 900 nm. The emission light from the spark plasma was collected using the fiber-SMA with the F-NO matcher attached to the entrance slit of the MS260i spectrograph, which was set at 25  $\mu\text{m}$  for the present study. The spectral lines spread over through the MS260i exit slit and were detected by the detector which was operated under full-vertical binning mode.

The optical beam deflection had a continuous HeNe laser beam (632.8 nm, 2 mW), it had a diameter of somewhat less than 1 mm as it passed near the spark breakdown region. The HeNe beam then was detected by the receiver unit which consisted of a fast PMT (2 ns rise time), a fiber optic cable (200  $\mu\text{m}$  core diameter), and a narrow band interference filter centered at 632.8. The receiver unit was located approximately 3 m from the region of interest. To preserve the quality of the laser beam throughout the experiments, the focal point was kept at a fixed location and the relative location of the HeNe beam was varied by translating the HeNe laser and the receiving unit vertically. The signals from the PMT detectors were fed into a fast Digital Phosphor Oscilloscope (Tektronix TDS35052). The scope was triggered by the signal from a PIN photodiode, which was used to detect the scattered Nd-Yag light from the focusing.

## **3. Results and Discussion:**

### ***3.1 Breakdown probability***

The breakdown probability reported here is defined as the number of successful breakdowns divided by the number of laser pulses used for each measurement. In the first experiment we looked at the effect of the focal length, (50 mm, 100mm, and 200 mm), on the breakdown probability observed for air. The experiment was carried out in quiescent air and using single laser shot. Thus, we were able to avoid the effects of the gas-dynamic mixing and entrainment of the surrounding gas and the pressure perturbation caused by the breakdown plasma. With a single shot we also avoid the effect of the metastable remnants produced by the prior pulse possibly being present in the focal volume for subsequent laser shots. The results with about 15% experimental uncertainty are shown in Fig. 1. It is clear that the breakdown probability increases systematically from zero to unity as the laser pulse energy increases. The focal length has a strong effect on both the breakdown threshold and the breakdown probability. For example, with the 50 mm focal length lens, the breakdown probability was about 2% at about 8.5 mJ and it became unity at about 12 mJ. While with the 200 mm focal length lens, 2% breakdown probability was measured at 20 mJ and a unity breakdown probability was observed at 43 mJ. Although it is not shown here, it was also observed that, the spark created by the 50 mm focal length lens was short, it occurred before the focal point and moved toward the laser. The spark created by the 200 mm focal length lens was very much longer. It occurred closer to the focal point and broke into a series of several small sparks moving along with the laser beam.

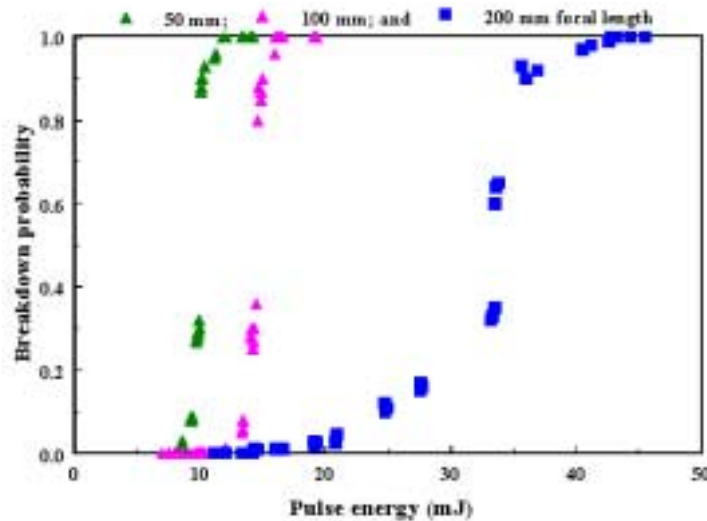


Figure 1. Breakdown probability as a function of the laser pulse energy: Effect of the focal length; (Laser-induced breakdown in air, 1064 nm wavelength, 5.5 ns pulse duration, single pulse, and 760 torr pressure)

To see how the focal length has such a strong effect on the breakdown probability it is useful to calculate the laser beam condition at the focal volume. For a Q-switched pulse of a

laser operating in a single longitudinal mode, the pulse energy of a temporal pulse shape that is Gaussian in time is given as

$$E(\tau) = E_{\max} \exp\left(-\tau^2/\tau_o^2\right), \quad (1)$$

Where  $E$  is the pulse energy (J),  $E_{\max}$  is the maximum laser energy,  $\tau$  is the time, and  $\tau_o$  is the time at which  $E(\tau_o) = E_{\max}/e$ , ( $e = 2.7183$ ). Let  $\tau_{FWHM}$  be the pulse duration (FWHM). Then  $\tau_o$  is calculated from the following relation:

$$\tau_o = \frac{\tau_{FWHM}}{2\sqrt{\ln 2}}; \quad (2)$$

the average laser energy,  $E_o$ , over  $\tau_o$  is given as

$$E_o = \frac{1}{\tau_o} \int_{-\infty}^{\infty} E(\tau) d\tau = \int_{-\infty}^{\infty} P_w \exp\left(-\tau^2/\tau_o^2\right) d\tau, \quad (3)$$

where  $P_w$  is the laser power (W); and  $P_w$  relates to  $E_o$  by the following:

$$P_w = \frac{E_o}{\tau_o \sqrt{\pi}}. \quad (4)$$

If the focal region of the beam is assumed to be cylindrical in shape, the spot size, in terms of radius,  $r$ , and length,  $l$ , is given as

$$r = \left(\frac{2\lambda}{\pi}\right) \left(\frac{f}{d}\right), \quad (5)$$

and

$$l = (\sqrt{\pi} - 1) \frac{\theta}{d} f^2, \quad (6)$$

and the electric field,  $F_E$  (in V/cm), and the photon flux,  $F_{ph}$  (in photon/cm<sup>2</sup>-s,) are

$$F_E = \left(\frac{4 P_w}{r^2 c}\right)^{1/2} = 11.55 \left(\frac{P_w^{1/2}}{r}\right) \quad (7)$$

$$F_{ph} = \frac{P_w \lambda}{\pi r^2 h c} = 1.7 \times 10^{18} \left(\frac{P_w}{r^2}\right) \quad (8)$$

Where  $f$  is the focal length,  $\lambda$  is the laser wavelength,  $d$  is the beam diameter,  $\theta$  is the beam divergence, and  $c$  is the velocity of light. For the present study,  $\lambda = 1.064 \mu\text{m}$ ,  $\theta = 0.5 \text{ mrad}$ , and  $d = 0.6 \text{ cm}$ . With pulse duration (FWHM) of 5.5 nanoseconds,  $\tau_0$  was calculated to be equal to 3.3 ns. For the range of  $E_0$  from 8 and 45 mJ, as used in this work, the calculated laser power, photon flux, irradiance, and electric field are tabulated in Table 1.

It is clear that, for the same laser pulse energy, the short focal length lens results in a much smaller focal volume, higher power density, higher photon fluxes, and stronger electric fields. Although it is possible that the diffusion loss out from the focal volume might be important for the shorter focal length, the differences in the electric field, the photon flux, and the energy density might be the significant factors controlling the production of the initial electrons leading to the electron cascading process.

Table 1. Laser energy and power for the present experiments

Focal length 200mm	50 mm	100mm	
Focal volume radius, ( $\mu\text{m}$ )	5.644	11.288	22.576
Focal volume length, ( $\mu\text{m}$ )	86.294	345.178	1380.712
Laser Energy, $E_0$ , of 8 mJ, (Power, $P_w = 1.36 \times 10^6 \text{ W}$ )			
Irradiance, ( $\text{W}/\text{cm}^2$ )	$1.36 \times 10^{12}$	$3.414 \times 10^{11}$	$8.537 \times 10^{10}$
Photon Flux, $F_{ph}$ , (Photons/ $\text{cm}^2$ -s)	$7.258 \times 10^{30}$	$1.814 \times 10^{30}$	$4.536 \times 10^{29}$
Electric field, $F_E$ , (V/cm)	$2.38 \times 10^7$	$1.19 \times 10^7$	$5.966 \times 10^6$
Laser Energy, $E_0$ , of 45 mJ (Power, $P_w = 7.695 \times 10^6 \text{ W}$ )			
Irradiance, ( $\text{W}/\text{cm}^2$ )	$7.69 \times 10^{12}$	$1.922 \times 10^{12}$	$4.805 \times 10^{11}$
Photon Flux, $F_{ph}$ , (Photons/ $\text{cm}^2$ -s)	$4.11 \times 10^{31}$	$1.027 \times 10^{31}$	$2.567 \times 10^{30}$
Electric field, $F_E$ , (V/cm)	$4.914 \times 10^7$	$2.813 \times 10^7$	$1.406 \times 10^7$

### 3.2 Spark energy

Using the arrangement for the two pyroelectric energy meters described previously, the transmitted energies through the focal volume, with and without breakdown, were measured. Data on the ratio of the transmitted energy to the pulse energy, ( $E_{tr}/E_0$ ), as a function of the pulse energy  $E_0$  are shown in Fig. 2. In general, the curves in Fig. 2 show that when  $E_0$  was below its threshold level, air was virtually transparent to the experimental laser wavelength, and the laser beam was transmitted through the focal volume without attenuation. When  $E_0$  increased to above its threshold level  $E_{tr}/E_0$  decreased drastically. This is because increasing the laser energy

will lead to gas breakdown, and the laser beam is attenuated due to the electron-ion inverse bremsstrahlung process, in which light is absorbed as a result of free-free transitions of the electrons in the field of the ions. The attenuation of the laser energy in the presence of breakdown is also attributed to the scatter of the laser light by the developing spark plasma. However, losses due to diffraction as well as the contribution of the reflected beam from the exit window that might add additional energy into the spark column are negligible [5,9], such the attenuation, therefore, can be considered to be due solely to the absorption by the spark.

Several significant features are observed from the results shown in Fig. 2. Firstly, it was shown that there was a large fluctuation in the spark energy and it decreased with the decreasing focal length and the increasing laser energy. Such the fluctuation can be attributed to the fluctuation of the electron density produced by the breakdown process, which depends on the laser wavelength, the incident laser energy and the beam quality including the condition by which the laser beam is focused. Secondly, the spark absorption depended strongly on the incident laser energy and about higher than 50% of the incident laser energy was absorbed even when the laser energy was just above the breakdown threshold range. This indicates that, after the start of breakdown, the free-electron grows rapidly to a large concentration that sufficiently absorbs most of the incident energy before the end of the laser pulse. Thus, the electron growth rate must be much faster the laser energy deposition rate. Thirdly, for the range of the laser energy used, after the  $E_{tr}/E_0$  decreased with the increasing pulse energy it started to level off or slightly increase. This indicates that the plasma was saturated. For the 50-mm focal lens, this condition occurred when the pulse energy was about 3 times of the breakdown threshold. For the 100-mm and 200 mm focal length lenses it was about 2 times and 1.5 times of the breakdown threshold, respectively. It is believed that, when the plasma reaches its saturation condition, the laser energy in the trailing edge of the laser pulse is able to go through the plasma. If more energy is added into the plasma, the plasma tends to expand its size instead of becoming denser or hotter

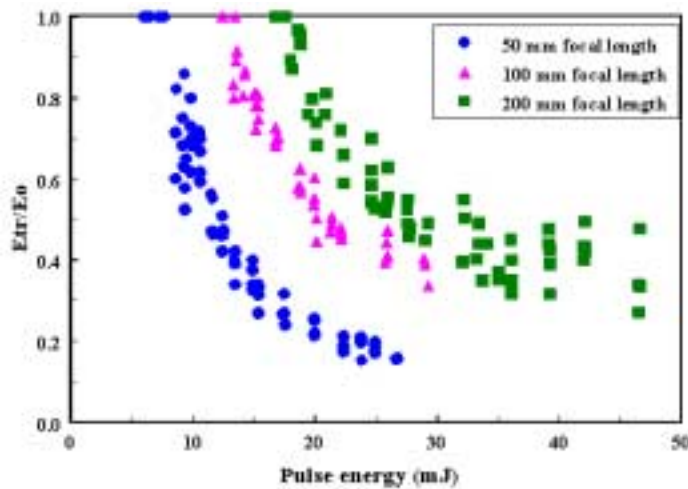


Figure 2. The transmitted energy through the laser spark in air:

Effect of the focal length; (1064 nm, 760 torr).

### 3.3 Spark Temperature

The temperatures reported here were measured using the two-line intensity ratio technique. If the plasma is assumed to be in thermal equilibrium the Boltzmann distribution can be used to calculate the population of the excited state as:

$$n_{oi} = n_o \frac{g_i}{Z} \exp\left(-\frac{E_i}{kT}\right) \quad (9)$$

Where  $n_{oi}$  is the population of the  $i^{\text{th}}$  excited state,  $g_i$  is the statistical weight of the excited state,  $Z$  is the partition function,  $E_i$  is the excitation energy,  $k$  is the Boltzmann constant, and  $T$  is the absolute temperature. The absolute intensity of the line emission is proportional to the population of the excited state and it can be written as:

$$I_{oi} \approx A_{oi} n_{oi} h\nu_{oi} = A_{oi} h\nu_{oi} n_o \frac{g_i}{Z} \exp\left(-\frac{E_i}{kT}\right) \quad (10)$$

Where  $A_i$  is the transition probability from  $o$  to  $i$  transition,  $h\nu_i$  is the energy of the transition from  $o$  to  $i$ . Thus, using the ratio of two line intensities with sufficiently different energies the temperature of the plasma can be determined:

$$\frac{I_2}{I_1} = \frac{A_2 g_2 \nu_2}{A_1 g_1 \nu_1} \exp\left(\frac{E_1 - E_2}{kT}\right) \quad (11)$$

or

$$T = \frac{E_1 - E_2}{k \ln \left[ \frac{A_1 g_1 \nu_1 I_2}{A_2 g_2 \nu_2 I_1} \right]} \quad (12)$$

In the temperature measurements the absolute intensities emitted from O I at 748.07 nm ( $A, [10^8, s^{-1}] = 0.226$ ,  $g=3$ ,  $E, [cm^{-1}] = 127292$ ) and 777.54 nm ( $A, [10^8, s^{-1}] = 0.340$ ,  $g=3$ ,  $E [cm^{-1}] = 86626$ ) were used. The emission line intensities at these two wavelengths are shown in Fig. 3. These lines were used because they are fairly sensitive emission lines, they have a small difference in the wavelength separation and are within spectral respond of the detector system but relatively large separation in the upper energy levels.

The spark temperature as a function of the spark energy (absorbed Energy) is shown in Fig. 4 showing the effect of the focal length. In general, the temperature increased rapidly from

$5 \times 10^4$  K when the spark energy increased up to about 15 mJ and it reached the saturation level when the spark energy was above 15 mJ. The saturation temperature of the spark produced with 50-mm focal length lens was  $1.6 \times 10^5$  K and it was about  $1.25 \times 10^5$  K for the spark created with 100-mm focal length lens. These temperatures are in agreement with those reported in the literature [15]. In addition, we also observed a large fluctuation in the spark temperature. The deviation of the spark temperature could vary by several thousand degrees compared to the average value depending on the focal length.

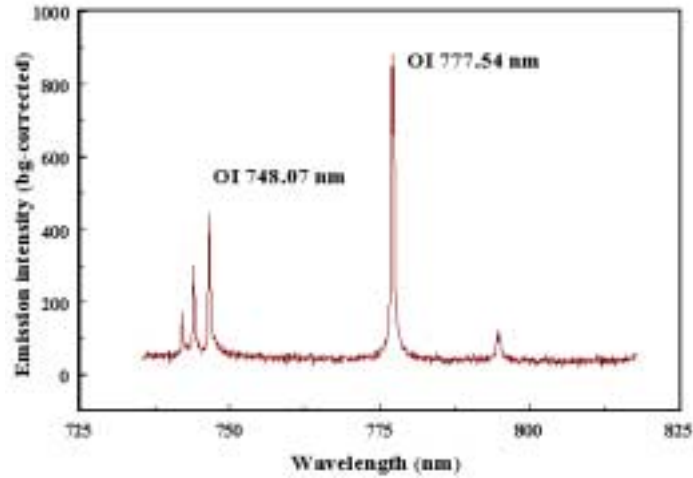


Figure 3. Space resolved emission intensity of laser spark in air; (absorbed energy equals to 17.09 mJ; 50 mm focal length; 760 torr, 1064 nm)

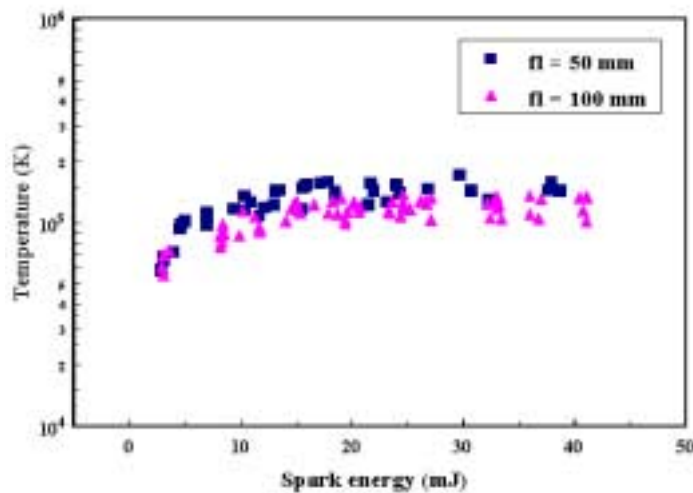


Figure 4. Temperature as a function of the absorbed energy:  
Effect of the focal length (760 Torrs, single pulse, 1064 nm)

### 3.4 Spark Evolution

We have made some preliminary measurements of the characteristics of the shock propagating out of the laser spark region using the beam deflection technique. When the detection beam interacts with the shock front it deflects at an angle  $\beta$  with respect to its undisturbed direction due to the effects of density, temperature, and ionization on the refractive index of the shock region. Thus, by measuring the deflection angle  $\beta$  and the sudden change in the PMT signal one should be able to identify the shock arrival time, the shock location, and the shock strength.

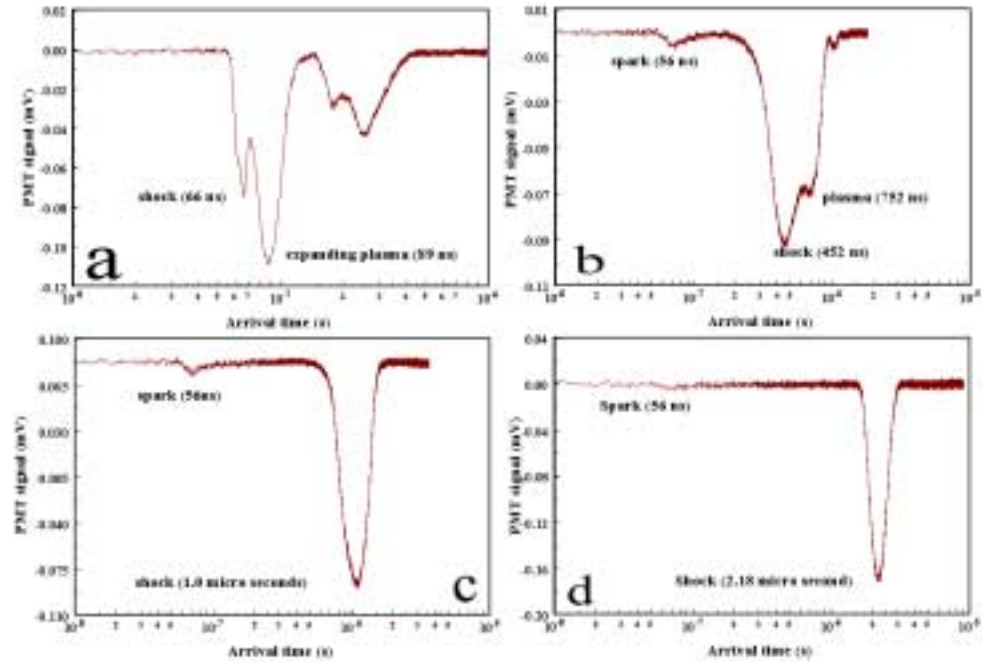


Figure 5. Evolution of the laser-induced spark shock wave 30 mJ; (a: laser beam was 0.4 mm, b: 0.8 mm, c: 1.2 mm, and d: 1.6 mm above the spark).

It is known from the previous sections that the laser spark temperature in the order of  $10^5$  to  $10^6$  K could be reached at the end of the laser pulse. Such the strongly overcompressed and overheated spark then forces the shock wave front to expand supersonically into the ambient gas producing the ionization of the gas on its path and increasing the spark plasma volume. Thus, the evolution of the laser spark must consist of many consecutive phases and processes starting

with the onset of the spark, the formation and the propagation of the shock wave front, the expansion of the spark volume and it is followed by the after-shock perturbation. Since the shock front speed is very much faster than that of the plasma expansion front, the shock will eventually detach from the plasma front at some point in the flow field and continues to expand into the unperturbed gas until the pressure equality with the gas is reached. Four typical traces of the PMT signals showing these phases are shown in Fig. 5. In this figure, the spark energy was 30 mJ. The HeNe beam was passing through four locations: 0.4, 0.8, 1.2, and 1.6 mm above the spark center and reached the receiver unit at about 10 mm above the fiber tip.

Figure 5a shows the evidence of the shock wave front, the expanding plasma front, and the after-shock pressure perturbation within the spark when the HeNe beam was 0.4 mm from the spark center. In this region the onset of the spark, the arrival times of the shock and the plasma fronts were not clearly distinguishable. The shock arrival time was 10 ns after the onset of the spark and it was overlapped with the onset of the laser spark. Immediately following the shock front was the expanding plasma front that reached the detection beam by only about 23 ns later. Figure 5b shows the evidence of the shock detachment when the shock front reaches to the location of 0.8 mm from the spark center. At this location, the onset of the laser spark and the arrival time of the shock front became obviously clear. The arrival time of the shock was about 400 ns after the onset of the spark and the plasma front just barely reached the HeNe beam 300 ns after the shock. After this location, the plasma expansion ceases. However, the shock front detaches the plasma volume and continues to expand as evidenced by the PMT traces shown in Figs. 5c and 5d for the case where the detection beam was 1.2 and 1.6 mm from the spark center. At these locations the plasma front did not reach the detection beam. The shock front, however, detached the spark plasma completely and reached the detection beam about 944 ns and 2.12  $\mu$ s, respectively, after the onset of the spark.

Typical results on the shock arrival time, the shock velocity and the shock mach number as a function of the shock radius are shown in Fig. 6. The shock arrival time increased rapidly with the shock radius. The effect of the spark energy on the shock arrival time is shown in Fig. 7. A linear relationship between the spark energy and the arrival time was obtained. For two levels of the spark energy reported here, the shock expansion was complete in the region of less than 4 mm and within the time frame of less than 5  $\mu$ s. The shock propagation velocity measured at 0.4 mm from the spark center was in the order of  $10^6$  cm/s and it decreased rapidly as the shock front moved. Such a supersonic propagation continued until the shock front expanded to 3.2 to 3.6 mm from its center, at which location the propagation has slowed down to the speed of sound in standard air. It is noticed that, since the diameter of the detection beam was in the order of 1 mm or less, we were not able to detect the arrival of the shock in the region less than 0.4 mm. It is expected that the shock velocity in this region is much higher than the results reported here.

#### 4. Conclusions

We have reported some preliminary results on the optical characterization of the laser spark in terms of the breakdown probability spark temperatures and spark evolution. The breakdown probability was found to depend strongly on the incident laser energy, the focal length and the gas pressure. Such the fluctuation in the gas breakdown event leads to a large deviation in the spark energy, the spark size, and the spark temperature. For ignition application, such large

fluctuations in the spark energy, the spark size, and the spark temperature indicate that not all breakdown events will lead to a successful ignition. Ignition will not occur if the spark size is not large enough to support the flame to grow or the deposited energy is less than the minimum ignition energy. On the other hand, if the deposited energy is excessively high it could lead to an increase in  $\text{NO}_x$  and other pollution species. The fluctuation in the time of the breakdown might be a problem if engines or engines with multiple cylinders require the ignition event at a specified location or time. Such a problem might become even more serious if synchronization of the ignition event for the cylinders is required. Some preliminary results the formation and the propagation of the shock wave front, the expansion of the spark volume, the after-shock perturbation, and the complete shock detachment were presented. Interpretation of the post shock signals is difficult, but the present data confirm that the gas is perturbed significantly, long after passage of the shock front. This period, which can extend hundreds of nanosecond to microseconds, may be important in the mixing of active reagents created by the early shock. Because the shock is weak outside a radius of a few mm, the active species may have to be carried out of the small shock heated region by these late pressure and density perturbations.

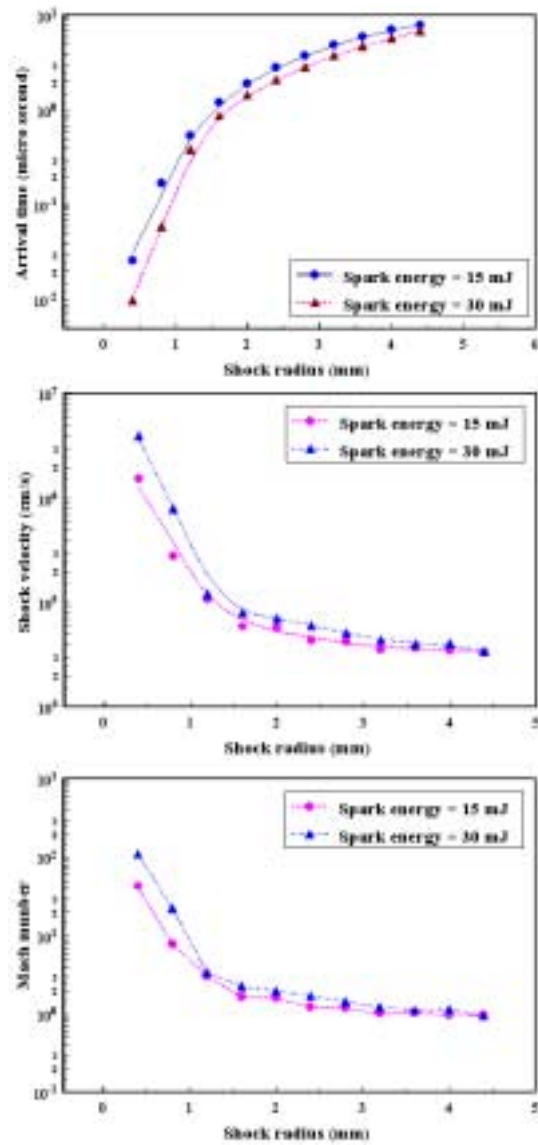


Figure 6. Shock arrival time, velocity, and Mach number as a function of the shock location

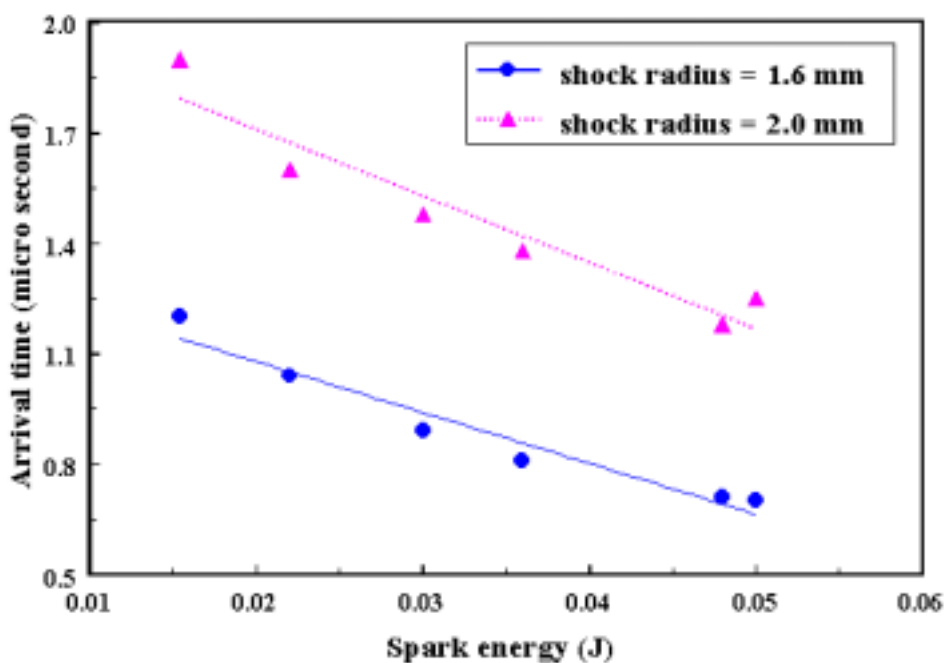


Figure 7. Shock arrival time as a function of the spark energy

## References

1. Turcu, I.C.E, Gower, M.C., and Huntington, P., "Measurement of KrF laser breakdown threshold in gases," *Optics Communications*, 134:66 (1997).
2. Peet, V.E., and Tsubin, R.V., "Multiphoton ionization optical breakdown of xenon in annular laser beams," *Optics Communications*, 134:69 (1997).
3. Weyl, G.M., "Physics of Laser Induced Breakdown: an Update," in *Laser-Induced Plasmas and Applications* (L.J. Radziemski and D.A. Cremers, Eds.), Marcel Dekker, New York, 1989, p. 1.
4. Phuoc T. X., "Laser spark ignition: Experimental determination of laser-induced breakdown thresholds of combustion gases," *Optics Communications*, 175, 419-423, (2000.)
5. Phuoc T. X., and White, "Experimental Studies of the Absorption and Emissions from Laser-Induced Spark in Combustible Gases," C., *Optics Communications*, 181, 353-359,
6. Lee, J.H., and Knystautas, R., "Laser Spark Ignition of Chemically Reactive Gases," *AIAA Journal*, 7:312 (1969).
7. Schmieder, R.W., "Laser spark ignition and extinction of a methane-air diffusion flame," *J. Appl. Phys.*, 52:3000 (1981).
8. Spiglanin, T.A., Mcilroy, A., Fournier, E.W., and Cohen, R.B., "Time-Resolved Imaging of Flame Kernels: Laser Spark Ignition of  $H_2/O_2/Ar$  Mixtures," *Combustion and Flame*, 102:310 (1995).

9. Syage, J.A., Fournier, E.W., Rianda, R., and Cohen, R.B., "Dynamics of flame propagation using laser-induced spark initiation: Ignition energy measurements," *J. Appl. Phys.*, 64:1499 (1988).
10. Ma, J.X., Alexander, D.R., and Poulain, D.E., "Laser Spark Ignition and Combustion Characteristics of Methane-Air Mixtures," *Combustion and Flame*, 112:492 (1998).
11. Lim, E.H., McLLroy, A., Ronney, P.D., and Syage, J.A., "Detailed Characterization of Minimum Ignition Energy of Combustible Gases Using Laser Ignition Sources," in *Transport Phenomena in Combustion*, (S.H. Chan, Ed.), Taylor & Francis, 1996, p. 176.
12. Morsy, M. H., Ko, Y.S., and Chung, S.H., "Laser-Induced Ignition Using a Conical Cavity in CH<sub>4</sub> –air Mixtures," *Combustion and Flame*, 119: 473, 1999.
13. Phuoc T. X., and White, F., "Laser-Induced Spark Ignition of CH<sub>4</sub>/Air Mixtures," *Combustion and Flame*, 119,203-216, (1999).
14. Chen, Y. L., Lewis, J.W.L., and Parigger, C., "Probability distribution of laser-induced breakdown and ignition of ammonia," *Journal of Quantitative Spectroscopy and Radiative Transfer*, 66, 41-53, (2000).
15. Chen, Y. L., Lewis, J.W.L., and Parigger, C., "Spatial and temporal profiles of pulsed laser-induced air plasma emissions," *Journal of Quantitative Spectroscopy and Radiative Transfer*, 67, 91-103 (2000).